

Article

In-Situ Generation of Nitrogen-Doped MoS₂ Quantum Dots Using Laser Ablation in Cryogenic Medium for Hydrogen Evolution Reaction

Fatemeh Shahi ¹, Parviz Parvin ^{1,*}, Seyedeh Zahra Mortazavi ², Ali Reyhani ², Mohtada Sadrzadeh ³, Ali Moafi ¹, Mahdi Ebrahimi ¹ and Mohammadreza Aghaei ^{4,5,*}

¹ Energy Engineering and Physics Department, Amirkabir University of Technology, Tehran 15119-43943, Iran

² Faculty of Science, Department of Physics, Imam Khomeini International University, Qazvin 34149-16818, Iran

³ Mechanical Engineering Department, University of Alberta, Edmonton, AB T6G 2R3, Canada

⁴ Department of Ocean Operations and Civil Engineering, Norwegian University of Science and Technology (NTNU), 6009 Ålesund, Norway

⁵ Department of Sustainable Systems Engineering (INATECH), University of Freiburg, 79110 Freiburg, Germany

* Correspondence: parvin@aut.ac.ir (P.P.); mohammadreza.aghaei@ntnu.no or aghaei@studysolar.uni-freiburg.de (M.A.)

Abstract: Here, nitrogen doped molybdenum disulfide quantum dots (N-MoS₂ QDs) are fabricated by making use of the pulsed laser ablation (PLA) process in liquid nitrogen (LN₂) as a dopant agent. In fact, LN₂ contributes the rapid condensation of the plasma plume to form MoS₂ QDs, optimizing the conditions for the synthesis of N-doped MoS₂ with p-type property. The structural/optical features of the synthesized products are studied using transmission electron microscopy (TEM), absorption spectroscopy, photoluminescence (PL) spectroscopy techniques, and X-ray photoelectron spectroscopy (XPS). The TEM image shows the creation of MoS₂ QDs with 5.5 nm average size. UV-vis and PL spectroscopy confirm the formation of N-MoS₂ QDs according to the dominant peaks. The Tuck plot gives a direct band-gap of 4.34 eV for MoS₂ QDs. Furthermore, XPS spectroscopy reveals Mo-N bonding, indicating nitrogen doping as evidence of p-type MoS₂ QDs. Thus, PLA provides a single-stage way to the clean and green synthesis of the MoS₂ QDs suspension without a need for high vacuum devices and additional chemical components. Regarding the pristine MoS₂, the N-MoS₂ QDs benefit from a low overpotential of -0.35 V at -10 mA/cm² per μ g alongside a low Tafel slope of 300 mV/dec. Subsequently, the lower R_{ct} value of N-MoS₂ QDs verifies the enhancement of the charge transfer kinetics mainly due to the elevated electronic conductivity. Furthermore, the quasi-rectangular cyclic voltammetry (CV) as well as the larger current window demonstrate a notable electrocatalytic activity. The former is based on the enhanced active sites in favor of N-MoS₂ QDs against other samples of interest. Thereby, it is discovered that the N-doped MoS₂ QD acts as an effective catalyst to notably improve the performance of the hydrogen evolution reaction (HER).

Keywords: MoS₂ quantum dots; pulsed laser ablation; liquid nitrogen; nitrogen doping; hydrogen evolution reaction



Citation: Shahi, F.; Parvin, P.; Mortazavi, S.Z.; Reyhani, A.; Sadrzadeh, M.; Moafi, A.; Ebrahimi, M.; Aghaei, M. In-Situ Generation of Nitrogen-Doped MoS₂ Quantum Dots Using Laser Ablation in Cryogenic Medium for Hydrogen Evolution Reaction. *Energies* **2023**, *16*, 455. <https://doi.org/10.3390/en16010455>

Academic Editor: Trong-On Do

Received: 27 November 2022

Revised: 23 December 2022

Accepted: 28 December 2022

Published: 31 December 2022



Copyright: © 2022 by the authors. Licensee MDPI, Basel, Switzerland. This article is an open access article distributed under the terms and conditions of the Creative Commons Attribution (CC BY) license (<https://creativecommons.org/licenses/by/4.0/>).

1. Introduction

Zero-dimensional quantum dots (QDs) benefit from distinctive optical and electrical properties arising from electron confinement in a nanometric space [1]. The molybdenum disulfide (MoS₂) sheets, a family of transition metal dichalcogenides (TMDs) and van der Waals material, are made up of Mo⁺⁴ ions tightly located between two layers of closely packed sulfide (S) anions, each layer having a thickness of 0.65 nm. MoS₂ QDs exhibit significant interest in both academic and industrial domains due to their notable properties based on the high surface area and quantum confinement effects. The synthesis of mono- and few-layer MoS₂ nanomaterials can be classified as a top-down process consisting of

mechanical exfoliation [2,3], chemical exfoliation [4–6], and laser thinning techniques [7]. In contrast, the bottom-up processes include chemical vapor deposition (CVD) [8–12] and pulsed laser deposition (PLD) [13–15]. Regarding CVD, a large scale deposition of MoS₂ is time-consuming, taking more than 24 h to complete the process [16]. However, the exfoliation and intercalation techniques may not be suitable for industrial applications owing to solvent dangerous precursors [15]. Furthermore, the cost of nanomaterial syntheses by the PLD method is relatively expensive due to the utilization of gas handling systems and vacuum chambers [17]. On the other hand, PLA of solid targets is a promising method for obtaining the stable suspensions of different nanostructures using a variety of liquids in a shorter fabrication time. Regarding the other methods, PLA in liquids is a one-step, versatile, straightforward, and economic technique for producing colloidal, agent-free, and extremely pure products that can be applied for industrial scale due to its green environmental applications [18–20].

There are a few reports available on the MoS₂ synthesis via the PLA technique in liquid media, that are tabulated in Table 1 alongside their specifications. However, there is no article addressing the synthesis of MoS₂ QDs in cryogenic media. The presence of LN₂ as a monolayer 2D fluid during the synthesis of MoS₂ and graphene oxide via the PLA method facilitates the rapid cooling of the laser-induced plasma [21,22]. Moreover, the optimum and easy conditions for in-situ doping nitrogen in nanostructures provide better results than other methods involving the expensive facilities and complex processes [23,24]. Yin et al. presented a technique to fabricate MoS₂ QDs for promoting cancer treatment regarding the photothermal events [25]. MoS₂ QDs were obtained within the colloidal suspensions using PLA of the commercial MoS₂ particles in liquid at 532 nm with pulse duration 7 ns, 50 mJ/pulse. This enhances the photocatalytic activity of MoS₂ QDs for the purpose of hydrogen (H₂) generation [1]. Mortazavi et al. introduced a unique, prompt, and easy method to exfoliate 2D material employing Nd:YAG laser pulses in LN₂ medium [21]. Furthermore, the p-type semiconductors are fabricated by the non-metal dopants, such as nitrogen, phosphorus, oxygen, etc., which substitute the S with N atoms. The materials' electronic features, catalytic activity, and the intrinsic conductivity are improved after the N doping [26–30]. Recently, we obtained the N-MoS₂ nanosheets (NSs) utilizing the PLA in a LN₂ medium, demonstrating its properties as p-type semiconductor [22]. On the other hand, H₂ as a combustion product benefits from high energy density and zero effect on the environment. Thus, it will be used as a future green and clean energy carrier in modern industry [31–35]. The HER ($2\text{H}^+ + 2\text{e}^- \rightarrow \text{H}_2$) relies on water's electrolysis in acidic media as a potential pathway to produce the hydrogen fuel [36,37]. According to the limitations, such as low thermal efficiency, unstable catalytic performance, and an extreme lack of cost-effective substitute catalysts during the process of HER, there is a need for novel electrocatalysts with good catalytic stability [1,13,36,38–40]. Thereby, controlling the morphology of material of interest and doping proper elements into MoS₂ represent the efficient approach of this work to increase the active sites and the corresponding conductivity leading to enhance HER activity. The latter arises from the edges of sulfur layers [40–42]. Hence, N doping to the MoS₂ leads to enhance the active sites by provoking the HER. In other words, the improving activity of S/Mo edges gives rise to the larger plane conductivity. Nanometric MoS₂ QDs with a few layers benefits from the greater density of edges compared to micrometric MoS₂ NSs with the same weight [26,40]. TMD monolayers have been doped using several techniques, including chemical doping, vacuum deposition, and ultrasonic dispersion [43,44]. To our knowledge, no report has addressed the doping of MoS₂ QDs simultaneously in their synthesis during the PLA in the cryogenic fluid.

Here, the N-MoS₂ QDs synthesis is reported using the PLA method in LN₂ in order to scale up HER performance probed by cyclic voltammetry, linear sweep voltammetry (LSV), and electrochemical impedance spectroscopy (EIS).

Table 1. Characteristics of PLA-synthesized MoS₂ QDs in different media.

Laser	Wavelength	Medium	Sizes	UV-Vis Peak [nm]	PL Peak [nm]	Ref.
Nd:YAG	1064, 532, 355 nm 6–7 ns	Water	2–30 nm	209.8 and 211.4	553–563	[45]
Nd:YAG	532 nm–7 ns	Acetonitrile	3–6 layers 5 to 20 nm	450	440 to 530	[1]
Ti:sapphire	800 nm–50 fs	Deionized (DI) water	1–120 nm 1–5 nm	$\lambda < 300$	340 to 450	[46]
Ti:sapphire	800 nm–150 fs	Diethylamine	1.8 nm	275	~420	[47]
Yb:KGW	1026 nm–170 fs	Water	-	-	448 nm	[48]
Nd:YAG	1064 nm–10 ns	LN ₂	5.5 nm	256 and 282 nm	300 to 450 nm	This work

2. Materials and Methods

MoS₂ powder (Aldrich, < 2 μ m, 99%) is utilized to fabricate the disk-shaped target using the spark plasma sintering (SPS) process at 20 MPa [49]. The MoS₂ QDs are generated by the ablation of Q-switched Nd:YAG laser in LN₂ (−195.8 °C), which acts as a cryogenic medium and dopant agent. Laser ablation is performed for 10 min exposure time (3000 shots) with laser line at 1064 nm and 5 Hz repetition rate alongside the pulse duration of 10 ns and 15 mJ/shot energy corresponding to the 1.5 J/cm laser fluence. Figure 1 illustrates the schematics of experimental setup in favor of the MoS₂ synthesis in LN₂. Initially, the MoS₂ bulk target is located at the bottom of an irradiation cryostat. After creating the vacuum in chamber, LN₂ is poured into the cryostat for the successive laser ablation. The LN₂ is continually injected into the cryostat until the condition of a thermal steady state is established. Then, a plano-convex lens ($f = 32$ mm) is employed to focus the laser beam on the target. The combustion materials and nitrogen gas are exited through the ventilation outlet. The residual LN₂ evaporates after the end of laser time exposure at the ambient temperature. Subsequently, the cryostat is injected with DI water-ethanol mixture to make a N-MoS₂ suspension.

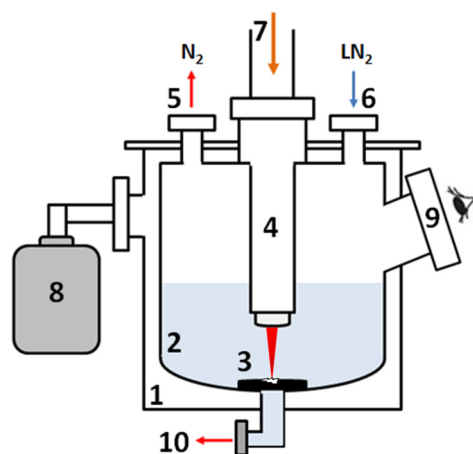


Figure 1. Diagram of the experimental argument: homemade irradiation cryostat to synthesize N-MoS₂ QDs in LN₂. 1—chamber of vacuum, 2—reservoir of LN₂, 3—mount of MoS₂ target, 4—beam guidance section, 5—outlet of ventilation (N₂ evaporator), 6—inlet of LN₂, 7—window of laser irradiation, 8—pump of rotary, 9—optical window for monitoring and 10—product yield location (outlet) [22].

A colloidal suspension of MoS₂ QDs is produced homogeneously by the MoS₂ target through PLA method followed by centrifugation. MoS₂ QDs are separated from the suspension through centrifugation, Hettich universal-320, for 30 min at 500 rpm. The supernatant is centrifuged again for an hour at 1000 rpm based on their weight difference

to obtain a transparent supernatant suspension. Finally, a very homogeneous colloidal suspension is obtained from the supernatant section containing a significant population of MoS₂ QDs.

The morphology and structure of end products are investigated using transmission electron microscopy; TEM, Philips CM30 microscope using a 150–200 kV acceleration voltage. The obtained suspension is drop-cast onto a copper (carbon-coated) TEM grid. The optical properties of produced N-MoS₂ QDs are examined via the UV–visible absorption spectrophotometer (Jenway 6715) operating in 200–1100 nm spectral range having a pulsed Xenon light source. The spectrometer benefits from a resolution of 1.5 nm, which is coupled with a dual silicon detector. The PL spectra are evaluated by a pulsed Xenon lamp ranging 200–1100 nm spectral range and a 1 nm spectral resolution equipped with a PMT array detector. Furthermore, an XPS spectrometer (Kratos, AXIS Ultra, Manchester, UK) is employed to determine the chemical composition. The deconvolution of peaks is performed using SDP software (version 7.0) following a peak fitting of 80% Gaussian–20% Lorentzian.

Electrochemical Measurements

Electrochemical measurements are carried out using an electrochemical instrument (Autolab PGSTAT302N, Metrohm, Netherlands) utilizing a conventional three-electrode configuration. All the electrodes are placed in 0.5 M H₂SO₄ aqueous solution as electrolyte. Saturated Ag/AgCl and platinum (Pt) electrodes are used as the reference electrode and the counter electrode, respectively [50]. Some articles reported graphite as the counter electrode [42]. The working electrodes are made of glassy carbon electrode (GCE) according to following the procedure: First, the pristine MoS₂ at 3 mg/mL concentration and the N-MoS₂ NSs at 3 µg/mL and QDs at 2 µg/mL concentrations are prepared in an ethanol-water solution at room temperature. Absolute ethanol and distilled water have a volume ratio of 2:1. Then, the mixed solution is dispersed using an ultrasonic bath for 30 min to create a homogeneous ink. Afterwards, 15 µL of a 5% Nafion solution is mixed with the ink and sonicated for 30 min to produce catalyst ink. After that, 10 µL of the ink is dropped onto the GCE surface (with a diameter of 3 mm, or ~7.1 mm²). Finally, the modified GCE is dried at room temperature. The CV measurements are carried out at a typical 20 mV/s scan rate to record the preliminary screening of the electrocatalytic activity of the N-MoS₂ QDs against N-MoS₂ NSs and pristine MoS₂ in an acidic medium. LSV measurements are carried out between –0.8 and 0 V at a scan rate of 2 mV/s in 0.5 M H₂SO₄ electrolyte utilizing Pt, Ag/AgCl and GCE electrodes. All potentials against the Ag/AgCl electrode are measured during the experiment. Potentials are calibrated with respect to the reversible hydrogen electrode (RHE). All reported potentials in 0.5 M H₂SO₄ are referenced to the RHE using the formula: $E(\text{RHE}) = E(\text{Ag}/\text{AgCl}) + 0.197 \text{ V}$. To ensure the repeatability of the experimental data, each measurement is carried out several times. Eventually, EIS is performed with a modulation amplitude of 5 mV. The frequency range for the EIS spectra spanned the range of 0.01 Hz–100 kHz. Here, we have shown that a small amount (in µg order) of N-MoS₂ NSs and QDs synthesized by the PLA method in LN₂ presents a very good catalytic effect with respect to traditional MoS₂ flakes in mg scale. Thus, the current density, *J*, appears per µg of catalytic ink in comparison.

3. Results

3.1. TEM Image

N-MoS₂ QDs are synthesized by the intercalation and exfoliation of MoS₂ target in LN₂ using PLA after the centrifugation. Figure 2a,b illustrate the N-MoS₂ QDs TEM images with 50 and 20 nm scales, respectively, and their size distribution. After centrifuging, most of the residual species in the supernatant suspension are the QDs with the average lateral sizes of 5.5 nm and ~2–10 nm size distribution. It is understood that the majority of QDs are arranged in the form of linear chains.

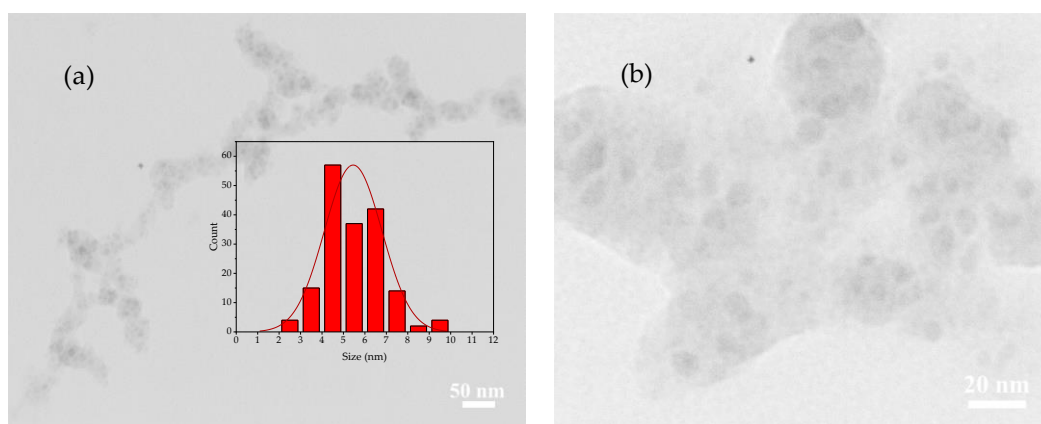


Figure 2. Typical TEM images of MoS₂ QDs (a) 50 nm scale and (b) 20 nm scale alongside size distribution, in inset (a), generated by pulsed laser at 1064 nm, 10 ns, 1.5 J/cm², and 5 Hz during cryogenic PLA synthesis process.

3.2. UV-Vis Spectroscopy and Tauc Plot

Figure 3a illustrates the normalized optical absorption spectrum of N-MoS₂ QDs. The excitonic peaks of material of interest appear at 256 and 282 nm ($\lambda < 300$ nm) in the near-UV region [40,46]. Conversely, the excitonic peaks are observed at A: 677, B: 627, C:457, and D: 402 nm in the form of nanosheets [22]. The position of A and B peaks is located towards the direct excitonic transitions, which can be shifted by changing the number of layers. Moreover, the position of C and D peaks arises from the direct transition that occurs by provoking the deep valence to the conduction bands [22]. However, the characteristic excitonic peaks notably vanish during the creation of N-MoS₂ QDs owing to the effects of quantum confinement and the quasi-continuous electronic energy band structure. Furthermore, a couple of dominant peaks appear in favor of N-MoS₂ QDs over the UV region, resembling the excitonic characteristics of MoS₂ QDs [51]. On the other hand, under UV light, the transparent QDs solution changes to a blue/green color, in accordance with the PL spectrum.

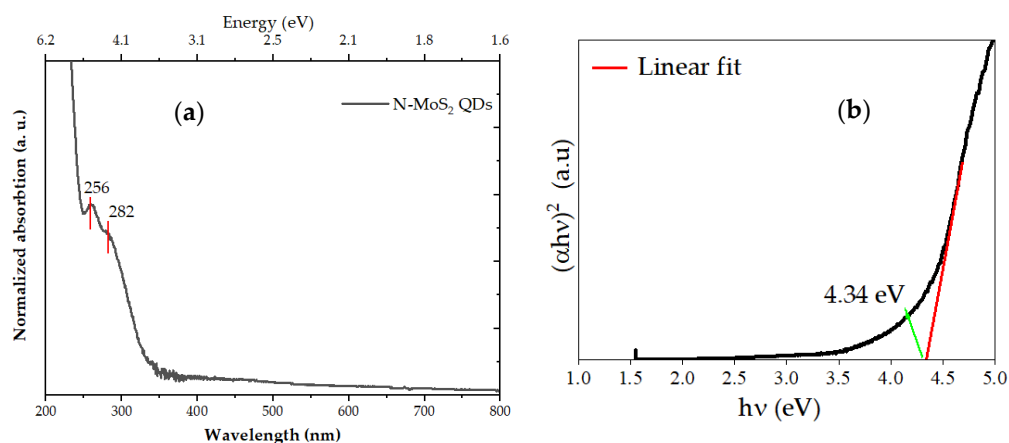


Figure 3. (a) Spectral absorbance of N-MoS₂ QDs synthesized by making use of Nd:YAG laser during cryogenic PLA synthesis process. (b) Corresponding Tauc plot indicating the optical band gap energy of N-MoS₂ QDs. Note that, in general, the doping N amount and the QDs size affect the bandgap of N-MoS₂ QDs. In fact, the band gap enlarges in favor of the smaller QDs.

The optical absorption coefficient (α) is calculated according to Equation (1) [52] based on Beer–Lambert law:

$$\alpha = 2.303 \frac{A}{d}, \quad (1)$$

where A is the absorbance $A = \log\left(\frac{I_0}{I}\right)$ value at the specific wavelength. The sample thickness, denoted by d , is assumed to be 1 cm, equivalent to the quartz cuvette thickness. Applying the UV-Vis data, the optical band gap of the N-MoS₂ QDs is calculated by virtue of Tauc formalism as follows [34,53,54]:

$$(\alpha h\nu)^{\frac{1}{n}} = B(h\nu - E_g), \quad (2)$$

where E_g , α , $h\nu$, and B are the optical band gap, the absorption coefficient and the incident photon energy, respectively. B is a constant value depending on the transition type. Depending on the transition type, n takes the values 2, 3/2, 1, and 1/2 for the forbidden indirect, forbidden direct, allowed indirect, and allowed direct, respectively. Here, the allowed direct transition with $n = 1/2$ is considered. In a direct-gap semiconductor, the photon emission takes place when an electron passes through an intermediate state with no momentum transfer [53,54].

Regarding the Tauc method, the absorption edge i.e., the extrapolation over the linear part of $(\alpha h\nu)^2$ depicts versus photon energy plot is a line that intersects the x -axis at E_g , where $(\alpha h\nu)^2 = 0$. This indicates the band gap energy of the MoS₂ QDs. Figure 3b displays the direct band gap of N-MoS₂ QDs. The material of interest benefits the band gap value of 4.34 eV, consistent with previous reports on MoS₂ QDs [55–57]. The reduction of MoS₂ sheets to the nanometric dimensions enlarges the material band gap according to the phenomenon of quantum confinement. The band gap in the specific cases of MoS₂ QDs is beneficial for the purpose of photo/electrocatalyst effect.

3.3. Photoluminescence Spectroscopy

Figure 4 illustrates the PL spectrum of N-MoS₂ QDs using the PLA after the laser exposure of with repetition rate of 5 Hz. The emission spectrum of MoS₂ QDs exhibits a pronounced emission at ~343.4 nm, in agreement with Ref. [46]. It is important to point out that the bulk MoS₂ does not exhibit PL emission, however it appears in favor of QDs and nanosheets [58]. In fact, the quantum confinement affects the electronic structure and the optical features of MoS₂ materials [59]. The induced defects of crystal structures also impact the PL spectrum of TMDs [60,61]. The formation of disordered MoO₃ regions within the MoS₂ crystal leads to PL quenching [62,63], while PL emission notably enhances due to the attendance of sulfur vacancies and the nitrogen doping at the defective sites.

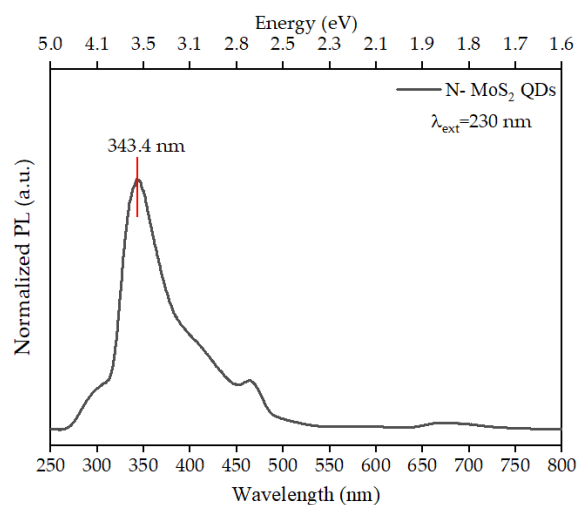


Figure 4. Typical PL spectrum of MoS₂ QDs using Nd: YAG laser in LN₂ under the excitation line at 230 nm. Note that, the PL peak appear at 343.4 nm and the shoulder at 460 nm exhibits second harmonic of λ_{ext} . The corresponding PL characteristic peak undergoes a spectral shift, as well as a shoulder, also appears due to the nitrogen doping.

3.4. XPS

Figure 5 depicts XPS spectra N-MoS₂ QDs for the peaks of N (1s), Mo (3 d), and S (2p) to determine the chemical components and bonding states according to the deconvolution of these spectra. Figure 5 shows the peaks at ~395 and ~397.1 eV, attributed to Mo 3p^{3/2} and N 1s peaks, respectively [28,35,64,65], as lucid evidence of the formation of Mo-N bonds [39]. In addition, the spectral overlap at 398.4 eV arises from the Mo-N bond [66], suggesting that the nitrogen atoms substitute S sites of MoS₂ QDs. The maximum peak is placed at 400.2 eV, corresponding to the N 1s peak arising from the Mo-N bond [28,67], indicating nitrogen doping during the PLA process within LN₂ [64]. A single peak appears at 401.7 eV (N-O) emphasizing the nitrogen monoxide (NO) adsorption on the skin surface of the MoS₂ [67,68]. Hereby, XPS results confirm the presence of N atoms replaced by S atoms in QDs of interest. Figure 5b displays the peaks at 228.8, and 232.7 eV indexing as doublet Mo⁺⁴ 3d^{5/2} and Mo⁺⁴ 3d^{3/2}, respectively [28,33,64,69]. Furthermore, the peak at 235.9 eV revealed in the Mo 3d region characterizes the high-valence Mo⁺⁶ most likely due to molybdenum oxide sulfide (MoO_{1.6}S_{1.9}) [70] or molybdenum oxides (MoO_x) [71]. The formation of oxide species is caused by the interaction of the nanosecond laser with the LN₂/target-MoS₂ interface out the air residual at the attendance of high-temperature gradient. Additionally, the energy peak at 237.7 eV is suggested from the Mo 3d orbital as molybdenum defective state [72], possibly due to the shift at higher energy binding during nitrogen doping. Moreover, the peaks at 226.6 [73] and 224.4 eV are correlated to the S 2s of Mo–S links in the Mo 3d region.

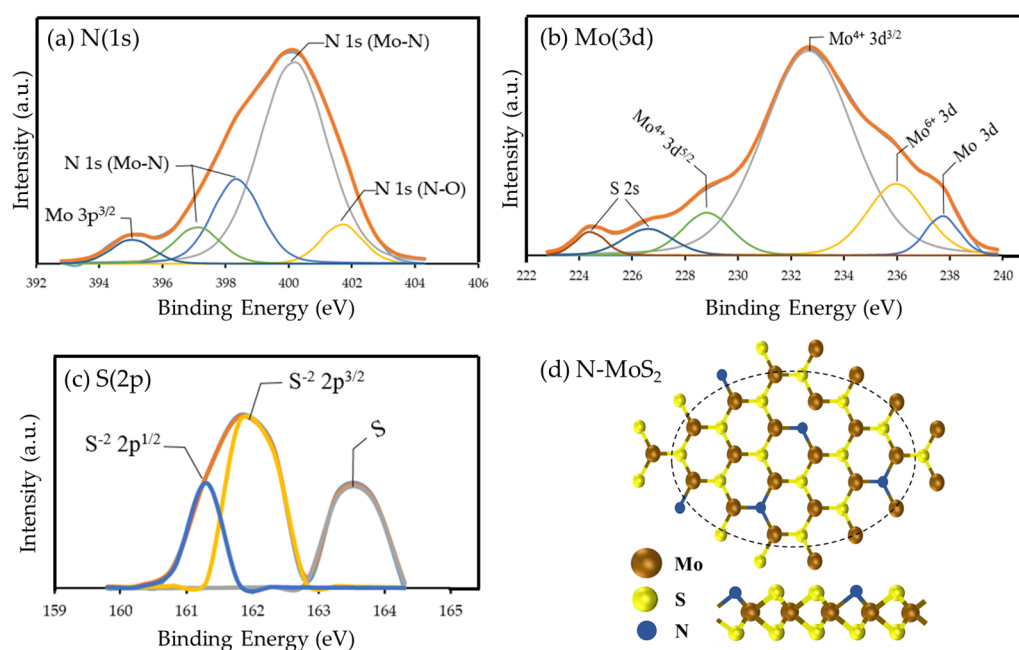


Figure 5. XPS spectra demonstrating energies of core binding. (a) N (1s) (b) Mo (3d), and (c) S (2p) of XPS spectra taken by N-MoS₂ QDs created by PLA in LN₂. The calibrated peak for all spectra is the C 1s peak, which is placed at 284.8 eV. The N (1s), Mo (3d), and S (2p) peaks are deconvoluted to identify the corresponding bonding states and chemical species following Shirley background subtraction alongside 80% Gaussian-20% Lorentzian fitting. Thus, the evidence of N-doping is obviously validated. (d) Typical scheme of top and side views of the covalent N-MoS₂ QDs, for instance, the formation of molybdenum nitride (MoN) and dimolybdenum nitride (Mo₂N) by PLA in LN₂. Note that, XPS attests the nitrogen doping lucidly takes place during process.

Figure 5c illustrates the peaks at 161.2 and 162 eV attributing the S 2p^{3/2} and S 2p^{1/2} of divalent sulfide ions (S²⁻), respectively [59]. Another peak at 163.6 eV is the characteristic of the S 2p of sulfur element [60,61]. The Mo 3d and S 2p peaks are shifted to the higher binding energies after nitrogen doping. This elucidates a higher chemical state owing to

the interaction between N, Mo, and S, approving that the nitrogen atoms are effectively doped into the QDs of interest [23,55].

3.5. HER Activity of the Nitrogen Doped MoS₂ QDs

3.5.1. Cyclic Voltammetry (CV)

The electrochemical performances of the pristine MoS₂, N-MoS₂ NSs and QDs are investigated in 0.5 M H₂SO₄ electrolyte by making use a standard three-electrode setup. The corresponding electrocatalytic activity of the N-MoS₂ QDs with respect to N-MoS₂ NSs and pristine MoS₂ is carried out by CV at a typical scan rate of 20 mV/s. Figure 6a displays the CV curves of materials of interest in comparison. The N-MoS₂ QD electrode demonstrates a notable electrochemical activity against N-MoS₂ NSs and pristine MoS₂ favoring HER performance. In fact, the background current of N-MoS₂ QDs gains the largest value and the pristine MoS₂ electrode shows the smallest one. In general, the background current is proportional to the surface area. The N-MoS₂ QDs electrode benefits a significant current response at a potential window of -0.29 to 0.40 V. On the other hand, the defects owing to the size, edge, and nitrogen doping of the N-MoS₂ QDs significantly enhance the active sites in order to accumulate the charges at the electrode/electrolyte interface as well as a pronounced pseudo-supercapacitive property due to the quasi-rectangular CV curve. We conclude that the numerous surface active sites and accessible edges, as well as large surface area create, the proper surface locations for the effective adsorption/desorption process of ions, resulting in a higher specific capacitance than other samples of interest.

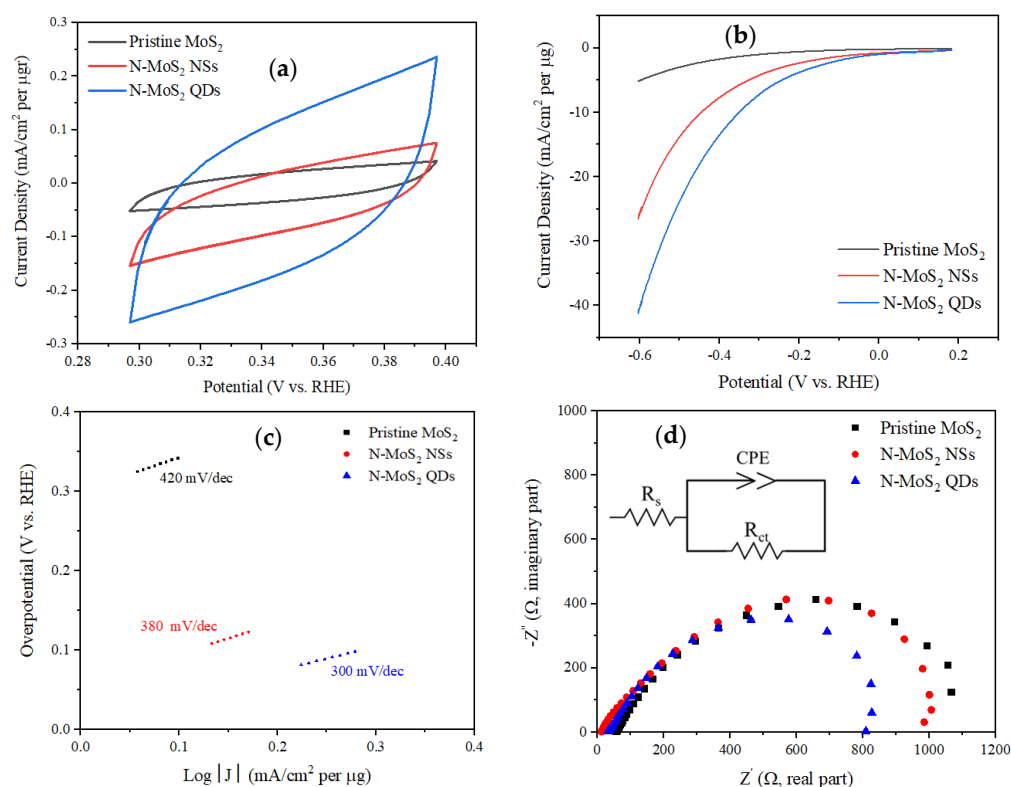


Figure 6. (a) Typical CV curves of the pristine MoS₂, N-MoS₂ NSs and N-MoS₂ QDs in 0.5 M H₂SO₄ electrolyte at a scan rate of 20 mV/s (b) LSV graphs in 0.5 M H₂SO₄ with scan rate of 2 mV/s, (c) corresponding Tafel plots of the pristine MoS₂, N-MoS₂ NSs and N-MoS₂ QDs and (d) Nyquist plots of the samples of interest in 0.5 M H₂SO₄. The inset shows the Randles equivalent circuit for the fitting of EIS data which R_s and CPE denote the solution resistance and constant phase element, respectively. Note that, the smaller Tafel plot slope indicates the larger catalytic activity for HER performance. Furthermore, N-MoS₂ QDs exhibit a less R_{ct} value due to a smaller semicircle diameter.

3.5.2. Linear Sweep Voltammetry (LSV)

LSV measurements are carried out in a 0.5 M H₂SO₄ solution with a scanning rate of 2 mV/s at room temperature to assess the catalytic activity in HER of the N-MoS₂ NSs and QDs using current density (J) versus applied voltage (V) as J–V curves. Figure 6b,c illustrate the obtained cathodic polarization curves and corresponding Tafel plots, respectively, in favor of three samples of interest, i.e., pristine MoS₂, N-MoS₂ NSs, N-MoS₂ QDs. It can be seen that the N-MoS₂ NSs and N-MoS₂ QDs benefit significantly lower onset overpotentials (η) against the pristine MoS₂. For instance, at a given current of -10 mA/cm^2 per μg , the η value of N-MoS₂ NSs and N-MoS₂ QDs are -0.45 and -0.35 V (versus RHE), respectively. The N-MoS₂ QDs reveal the lowest value of onset potential, indicating outstanding HER activity. Additionally, as shown in Figure 6b, the cathodic current densities per μg of N-MoS₂ NSs and N-MoS₂ QDs ($\eta = 0.6$ V) are obtained as 26.25 and 41.42 mA/cm^2 per μg , respectively. These values are five and eight times greater than that of the pristine MoS₂ (5.2 mA/cm^2 per μg). Thereby, the HER enhancement is verified in favor of N-MoS₂ NSs and N-MoS₂ QDs according to LSV spectra.

On the other hand, Tafel slope is an essential property of the electrocatalysts materials to show the kinetics of the HER process. The Tafel slope defines the overpotential increment corresponding to the higher reaction rate by a factor of ten. This is determined by the magnitude of the change in the activation energy for a given increase of the larger overpotential. A low Tafel slope corresponds to higher HER activity. In fact, a smaller voltage must be applied to obtain a given current according to the lower Tafel slope. Thus, more current can be produced with less power consumption [74]. The Tafel plots in Figure 6c match the Tafel equation $\eta = b \times \log j + a$, where η and J ascertain the overpotential and the current density, respectively. Furthermore, a and b denote to be a constant and the Tafel slope, respectively. The values of the Tafel slope for pristine MoS₂, N-MoS₂ NSs and N-MoS₂ QDs are determined to be ~ 420 , ~ 380 , and ~ 300 mV/dec, respectively. The strongest HER activity appears in favor of the N-MoS₂ QDs with the lowest Tafel slope. Although the Tafel slope of N-MoS₂ NSs is larger than that of N-MoS₂ QDs, the HER activity remains higher than that of pristine MoS₂. Hence, according to Figure 6c, the N-MoS₂ NSs and N-MoS₂ QDs exhibit significant HER activities, which arise from corresponding small Tafel slopes. Note that the N-MoS₂ QDs benefit from the optimal HER activity among the samples of interest.

3.5.3. Electrochemical Impedance Spectroscopy (EIS)

The HER catalytic kinetics of the catalysts are assessed by making use of EIS measurements according to the values of charge-transfer resistance (R_{ct}) in Nyquist plots. EIS is a powerful technique that allows separate analyses of stages of charge transfer in terms of different alternating current (AC) frequencies typically, here 0.01 Hz–100 kHz. Information about the electrochemical reactions regarding the surface and material properties of electrodes can be ascertained using the EIS measurement. Impedance is a measure of the ability of a circuit to resist the flow of electrical current. Impedance is measured in EIS by applying a small excitation signal that is an AC potential to an electrochemical system and the subsequent recording of the AC response. Impedance is composed of a real and an imaginary part. Each point on a Nyquist plot is the imaginary versus the real impedance at any frequency. Higher frequencies are on the left side and low frequencies are located on the right side of the Nyquist plot. As result, R_{ct} varies with frequency. We have obtained the value of R_{ct} , indicating the rate of charge exchange on the electrode-solution interface. Figure 6d displays that the N-MoS₂ QDs notably show a smaller semicircle diameter, implying a lower R_{ct} against those of N-MoS₂ NSs and pristine MoS₂. The inset of Figure 6d illustrates the Randles equivalent circuit for the fitting of EIS data. Table 2 tabulates the fitting of EIS data utilizing a Randles circuit to determine R_{ct} values alongside LSV, Tafel slope data, and the corresponding parameters, i.e., V and J . The R_{ct} of the N-MoS₂ QDs electrode at -0.5 V overpotentials is given as $0.897 \text{ k}\Omega$, which is lower than that of N-MoS₂ NSs ($1.131 \text{ k}\Omega$) and pristine MoS₂ ($1.162 \text{ k}\Omega$), indicating an enhanced HER kinetics

accompanying the faster reaction rate takes place in favor of N-MoS₂ QDs. Hence, the low R_{ct} value for QDs directly evidences the faster charge transport between N-MoS₂ QDs and electrolyte interface, leading to effective proton-electron recombination.

Table 2. Electrochemical characteristics of pristine MoS₂, N-MoS₂ NSs and QDs Electrodes.

Sample	Overpotential (V) at −4 mA/cm ² per μg	Overpotential (V) at −10 mA/cm ² per μg	J (mA/cm ² per μg) at η = 0.6 V	Tafel Slope (mV/dec)	R _{ct} (kΩ)
Pristine MoS ₂	−0.55	-	5.20	420	1.162
N-MoS ₂ NSs	−0.29	−0.45	26.25	380	1.131
N-MoS ₂ QDs	−0.20	−0.35	41.42	300	0.897

4. Discussion

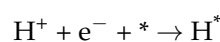
The synthesis of MoS₂ QDs, structures with nanometric lateral dimensions, is more difficult and necessitates the use of the similar techniques, such as reverse micelle synthesis or solvothermal reduction of (NH₄)₂MoS₄ with hydrazine at the attendance poly(vinylpyrrolidone) [23,24]. On the other hand, given their high price, Pt, Pd, and Rh (metallic catalysts), as the most effective electro-catalysts for the HER application, are strongly limited in large scale [40]. Here, it is demonstrated that the generation of N doped MoS₂ QDs with average size of 5.5 nm is easily carried out using PLA of bulk MoS₂ target in cryogenic nitrogen medium. In comparison to N-MoS₂ QDs using the sintering/etching/exfoliation method [40], the PLA method benefits single-step, time-saving, and doping during the synthesis process. Thereby, this method opens a straightforward way for improving the HER activity of catalysts according to the layered transition metal dichalcogenides for the first time. The experimental results above suggest N-MoS₂ QDs are successfully synthesized by virtue of the PLA method in LN₂. The TEM, UV-Vis, Tauc plot, PL, and XPS results lucidly demonstrate that LN₂ is a suitable cryogenic medium for the formation of in-situ N-MoS₂ QDs. The N bonding enhances the density of states close to the Fermi level, where more active sites are available for hydrogen adsorption [64]. Furthermore, the synthesized N-MoS₂ QDs exhibit a strong photoluminescence emission at ~343.4 nm after UV excitation at 230 nm.

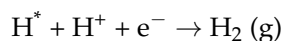
In other words, the N-MoS₂ QDs formation mechanism relies on the pulsed laser-induced thermal shock waves and interlayer position of N₂ causes to exfoliate flakes due to high temperature gradient. Subsequently, the sudden and rapid expansion that occurs during laser irradiation leads to a phase transition from liquid to gaseous [21,22]. Figure 5d depicts the covalent N-doping of MoS₂ QDs during the synthesis of PLA in cryogenic liquid-LN₂, demonstrating the replacement of N at the S locations. Naturally, there is a strong hybridization between the Mo-d states and the N-p as well as S-p states [22]. In fact, the covalent N-doping and the compressive strain in MoS₂ ignite the plasma in nitrogen gas that gives rise to the effective p-type doping of MoS₂ [75], in agreement with the findings of the present technique. On the other hand, the Hall effect proves the N-MoS₂ QDs to be p-type semiconductors. We have previously carried out the Hall effect to examine the semiconductor type of MoS₂ NSs [22]. A similar effect appears here for N-MoS₂ QDs too.

Typically, the HER mechanism on the catalyst surface can be accomplished according to Volmer discharge, Heyrovsky desorption, and Tafel combination reactions [36] in which the competitive events for hydrogen atoms, such as adsorption and desorption, take place at the catalyst to match with HER acceleration. According to HER electrocatalysts in acidic media, the Volmer–Heyrovsky mechanism has reported [34].

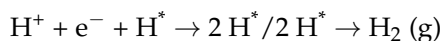
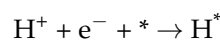


The creation of the H₂ molecule from the adsorbed H atoms can occur via two different initial pathways in the Volmer–Heyrovsky reactions:





where three simple pathways are used to form the hydrogen in the Volmer–Tafel reactions:



where the * denotes the active sites of the N-doped MoS₂ QDs as electrocatalysts, and H* indicates intermediates on the electrode's surface.

Thereby, nitrogen-doped MoS₂ QDs are simultaneously synthesized during the PLA process as a clean and green technique that introduces an efficient catalyst for hydrogen production. To better understand the importance of nitrogen doping MoS₂ QDs as a more effective catalyst, the following mechanisms are proposed. After nitrogen-doping, the density of electrons increases surrounding active sites at the doping positions due to the critical role of nitrogen atoms as the electron donors. This can improve the catalytic HER performance favoring the material of interest [33]. Hereby, the charge transfer process facilitates the higher electron density near the active sites. Moreover, these can lead to a balanced hydrogen population [36]. Our preliminary experiments on HER shows the effective feature of N-MoS₂ QDs catalytic activity to elevate hydrogen generation arising from excessive active sites in accordance with the reduction of MoS₂ size through the synergetic reactions. It is worth noting, the higher HER activity arises from both the exposed Mo active sites owing to S defects and the improved electron density state of S atoms caused by nitrogen doping [76]. Thereby, the N-MoS₂ QDs benefit higher HER activity than other samples of interest due to more active edge sites in order to ease the electron/ion transfer during the reaction.

5. Conclusions

The creation of N-MoS₂ QDs in the cryogenic medium is reported for the first time. This product is the nitrogen-doped QDs in 5.5 nm size as p-type semiconductors because those are synthesized in liquid nitrogen. Here, the Nd:YAG laser shots at 1064 nm focus on MoS₂ solid target in LN₂ medium. The target surface can be treated with laser-induced plasma to produce reactive sites that scale up nitrogen bonding and result in selective functionalization. Note that the process of nitrogen doping takes place during synthesis simultaneously. In fact, LN₂ acts as a dopant agent as well as the liquid medium for rapid plasma cooling to create QDs. It is important to note that the N-MoS₂ QDs are produced after optimizing variables, including the number of laser shots, irradiation time, and laser wavelength. The TEM image demonstrates N-MoS₂ QDs with a 5.5 nm distribution size. Moreover, the UV-Vis shows spectral absorbance in the range of $\lambda < 300$ nm, which is attributed to N-MoS₂ QDs having a 4.34 eV band gap according to the Tuck plot. Furthermore, the XPS spectra emphasize the N-doped MoS₂ QDs based on the deconvolution of spectra. The N-MoS₂ QDs synthesized by this method in cryogenic fluid benefit from a fast, flexible, one-stage, and chemically pollution-free process, making it easy to collect the products alongside in-situ doping. This approach could provide a new opportunity to fabricate several intriguing, highly active catalysts in favor of HER performance. In fact, one of the most promising applications of N-MoS₂ arises from its ability as a low-cost catalyst to replace expensive noble metal catalysts such as Pt during photo/electrocatalytic activities to generate hydrogen for the purpose of energy. Hence, it is shown that N-MoS₂ QDs contribute to enhancing the hydrogen evolution reactions, demonstrating eight times greater performance over the traditional MoS₂ ones. Eventually, we examine active electrocatalysts based on the PLA method to form the nitrogen-doped MoS₂ as p-type QDs in order to speed up the HER performance.

Author Contributions: Conceptualization, P.P., S.Z.M. and F.S.; methodology, P.P., S.Z.M. and F.S.; software, F.S. and A.R.; validation, P.P., S.Z.M., F.S. and A.R.; formal analysis, F.S., A.M. and M.E.; investigation, P.P., S.Z.M., M.S., M.A. and A.R.; resources, P.P. and M.A.; data curation, P.P., F.S. and A.R.; writing—original draft preparation, P.P. and F.S.; writing—review and editing, P.P., S.Z.M., F.S., A.R., M.S., A.M. and M.A.; visualization, P.P., S.Z.M., F.S. and A.R.; supervision, P.P., M.S. and S.Z.M.; project administration, P.P.; funding acquisition, P.P. and M.A. All authors have read and agreed to the published version of the manuscript.

Funding: This work is funded by the corresponding authors.

Data Availability Statement: Not applicable.

Acknowledgments: We appreciate Tarkib gas Alvand's general manager (Parviz Parvin) for technical supports. We are thankful to Behnam Eshghi for his assistance in electrochemical measurements.

Conflicts of Interest: The authors declare no conflict of interest.

References

1. Baldovi, H.G.; Latorre-Sánchez, M.; Esteve-Adell, I.; Khan, A.; Asiri, A.M.; Kosa, S.A.; Garcia, H. Generation of MoS₂ quantum dots by laser ablation of MoS₂ particles in suspension and their photocatalytic activity for H₂ generation. *J. Nanopart. Res.* **2016**, *18*, 240. [[CrossRef](#)]
2. Liu, K.-K.; Zhang, W.; Lee, Y.-H.; Lin, Y.-C.; Chang, M.-T.; Su, C.-Y.; Chang, C.-S.; Li, H.; Shi, Y.; Zhang, H. Growth of large-area and highly crystalline MoS₂ thin layers on insulating substrates. *Nano Lett.* **2012**, *12*, 1538–1544. [[CrossRef](#)] [[PubMed](#)]
3. Huang, Y.; Wu, J.; Xu, X.; Ho, Y.; Ni, G.; Zou, Q.; Koon, G.K.W.; Zhao, W.; Neto, A.C.; Eda, G. An innovative way of etching MoS₂: Characterization and mechanistic investigation. *Nano Res.* **2013**, *6*, 200–207. [[CrossRef](#)]
4. Eda, G.; Yamaguchi, H.; Voiry, D.; Fujita, T.; Chen, M.; Chhowalla, M. Photoluminescence from chemically exfoliated MoS₂. *Nano Lett.* **2011**, *11*, 5111–5116. [[CrossRef](#)]
5. Hernandez, Y.; Nicolosi, V.; Lotya, M.; Blighe, F.M.; Sun, Z.; De, S.; McGovern, I.; Holland, B.; Byrne, M.; Gun'Ko, Y.K. High-yield production of graphene by liquid-phase exfoliation of graphite. *Nat. Nanotechnol.* **2008**, *3*, 563. [[CrossRef](#)]
6. Novoselov, K.S.; Geim, A.K.; Morozov, S.V.; Jiang, D.; Zhang, Y.; Dubonos, S.V.; Grigorieva, I.V.; Firsov, A.A. Electric field effect in atomically thin carbon films. *Science* **2004**, *306*, 666–669. [[CrossRef](#)]
7. Castellanos-Gomez, A.; Barkelid, M.; Goossens, A.; Calado, V.E.; van der Zant, H.S.; Steele, G.A. Laser-thinning of MoS₂: On demand generation of a single-layer semiconductor. *Nano Lett.* **2012**, *12*, 3187–3192. [[CrossRef](#)]
8. Gong, Y.; Li, B.; Ye, G.; Yang, S.; Zou, X.; Lei, S.; Jin, Z.; Bianco, E.; Vinod, S.; Yakobson, B.I. Direct growth of MoS₂ single crystals on polyimide substrates. *2D Mater.* **2017**, *4*, 021028. [[CrossRef](#)]
9. Li, H.; Wu, H.; Yuan, S.; Qian, H. Synthesis and characterization of vertically standing MoS₂ nanosheets. *Sci. Rep.* **2016**, *6*, 21171. [[CrossRef](#)]
10. Yu, Y.; Li, C.; Liu, Y.; Su, L.; Zhang, Y.; Cao, L. Controlled scalable synthesis of uniform, high-quality monolayer and few-layer MoS₂ films. *Sci. Rep.* **2013**, *3*, 1866. [[CrossRef](#)]
11. Zhan, Y.; Liu, Z.; Najmaei, S.; Ajayan, P.M.; Lou, J. Large-area vapor-phase growth and characterization of MoS₂ atomic layers on a SiO₂ substrate. *Small* **2012**, *8*, 966–971. [[CrossRef](#)]
12. Deokar, G.; Vignaud, D.; Arenal, R.; Louette, P.; Colomer, J.-F. Synthesis and characterization of MoS₂ nanosheets. *Nanotechnology* **2016**, *27*, 075604. [[CrossRef](#)] [[PubMed](#)]
13. Wang, R.; Shao, Q.; Yuan, Q.; Sun, P.; Nie, R.; Wang, X. Direct growth of high-content 1T phase MoS₂ film by pulsed laser deposition for hydrogen evolution reaction. *Appl. Surf. Sci.* **2020**, *504*, 144320. [[CrossRef](#)]
14. Loh, T.A.; Chua, D.H. Pulsed laser fabricated few-layer MoS₂ on silver. *Chem. Phys. Lett.* **2014**, *610*, 284–287. [[CrossRef](#)]
15. Serna, M.I.; Moreno, S.; Higgins, M.; Choi, H.; Minary-Jolandan, M.; Quevedo-Lopez, M.A. Growth parameter enhancement for MoS₂ thin films synthesized by pulsed laser deposition. *Phys. Status Solidi C* **2016**, *13*, 848–854. [[CrossRef](#)]
16. Kang, K.; Xie, S.; Huang, L.; Han, Y.; Huang, P.Y.; Mak, K.F.; Kim, C.-J.; Muller, D.; Park, J. High-mobility three-atom-thick semiconducting films with wafer-scale homogeneity. *Nature* **2015**, *520*, 656–660. [[CrossRef](#)] [[PubMed](#)]
17. Hu, J.; Zabinski, J.S.; Sanders, J.H.; Bultman, J.E.; Voevodin, A.A. Pulsed laser syntheses of layer-structured WS₂ nanomaterials in water. *J. Phys. Chem. B* **2006**, *110*, 8914–8916. [[CrossRef](#)]
18. Barcikowski, S.; Devesa, F.; Moldenhauer, K. Impact and structure of literature on nanoparticle generation by laser ablation in liquids. *J. Nanopart. Res.* **2009**, *11*, 1883. [[CrossRef](#)]
19. Yang, G. Laser ablation in liquids: Applications in the synthesis of nanocrystals. *Prog. Mater. Sci.* **2007**, *52*, 648–698. [[CrossRef](#)]
20. Mortazavi, S.Z.; Parvin, P.; Reyhani, A.; Golikand, A.N.; Mirershad, S. Effect of laser wavelength at IR (1064 nm) and UV (193 nm) on the structural formation of palladium nanoparticles in deionized water. *J. Phys. Chem. C* **2011**, *115*, 5049–5057. [[CrossRef](#)]
21. Mortazavi, S.Z.; Parvin, P.; Reyhani, A. Fabrication of graphene based on Q-switched Nd: YAG laser ablation of graphite target in liquid nitrogen. *Laser Phys. Lett.* **2012**, *9*, 547. [[CrossRef](#)]

22. Shahi, F.; Parvin, P.; Mortazavi, S.Z.; Reyhani, A.; Soltannia, B.; Sadrzadeh, M.; Moradi, H.; Ojaghloo, A.; Moafi, A. Synthesis, Characterization, and Typical Application of Nitrogen-Doped MoS₂ Nanosheets Based on Pulsed Laser Ablation in Liquid Nitrogen. *Phys. Status Solidi A* **2022**, *219*, 2100677. [[CrossRef](#)]
23. Wilcoxon, J.; Newcomer, P.; Samara, G. Synthesis and optical properties of MoS₂ and isomorphous nanoclusters in the quantum confinement regime. *J. Appl. Phys.* **1997**, *81*, 7934–7944. [[CrossRef](#)]
24. Zong, X.; Na, Y.; Wen, F.; Ma, G.; Yang, J.; Wang, D.; Ma, Y.; Wang, M.; Sun, L.; Li, C. Visible light driven H₂ production in molecular systems employing colloidal MoS₂ nanoparticles as catalyst. *Chem. Comm.* **2009**, 4536–4538. [[CrossRef](#)]
25. Yin, W.; Yan, L.; Yu, J.; Tian, G.; Zhou, L.; Zheng, X.; Zhang, X.; Yong, Y.; Li, J.; Gu, Z. High-throughput synthesis of single-layer MoS₂ nanosheets as a near-infrared photothermal-triggered drug delivery for effective cancer therapy. *ACS Nano* **2014**, *8*, 6922–6933. [[CrossRef](#)]
26. Xiao, W.; Liu, P.; Zhang, J.; Song, W.; Feng, Y.P.; Gao, D.; Ding, J. Dual-Functional N Dopants in Edges and Basal Plane of MoS₂ Nanosheets Toward Efficient and Durable Hydrogen Evolution. *Adv. Energy Mater.* **2017**, *7*, 1602086. [[CrossRef](#)]
27. Enejekwu, F.M.; Zhang, Y.; Ezech, C.I.; Zhao, H.; Xu, M.; Besley, E.; George, M.W.; Besley, N.A.; Do, H.; Wu, T. N-doping enabled defect-engineering of MoS₂ for enhanced and selective adsorption of CO₂: A DFT approach. *Appl. Surf. Sci.* **2021**, *542*, 148556. [[CrossRef](#)]
28. Liu, Q.; Weijun, X.; Wu, Z.; Huo, J.; Liu, D.; Wang, Q.; Wang, S. The origin of the enhanced performance of nitrogen-doped MoS₂ in lithium ion batteries. *Nanotechnology* **2016**, *27*, 175402. [[CrossRef](#)]
29. Hu, C.; Yuan, C.; Hong, A.; Guo, M.; Yu, T.; Luo, X. Work function variation of monolayer MoS₂ by nitrogen-doping. *Appl. Phys. Lett.* **2018**, *113*, 041602. [[CrossRef](#)]
30. Fan, X.; Huang, Y.; Wang, H.; Zheng, F.; Tan, C.; Li, Y.; Lu, X.; Ma, Z.; Li, Q. Efficacious nitrogen introduction into MoS₂ as bifunctional electrocatalysts for long-life Li-O₂ batteries. *Electrochim. Acta* **2021**, *369*, 137653. [[CrossRef](#)]
31. Yasin, G.; Ibrahim, S.; Ibraheem, S.; Ali, S.; Iqbal, R.; Kumar, A.; Tabish, M.; Slimani, Y.; Nguyen, T.A.; Xu, H. Defective/graphitic synergy in a heteroatom-interlinked-triggered metal-free electrocatalyst for high-performance rechargeable zinc–air batteries. *J. Mater. Chem. A* **2021**, *9*, 18222–18230. [[CrossRef](#)]
32. Yasin, G.; Arif, M.; Ma, J.; Ibraheem, S.; Yu, D.; Zhang, L.; Liu, D.; Dai, L. Self-templating synthesis of heteroatom-doped large-scalable carbon anodes for high-performance lithium-ion batteries. *Inorg. Chem. Front.* **2022**, *9*, 1058–1069. [[CrossRef](#)]
33. Yang, Q.; Wang, Z.; Dong, L.; Zhao, W.; Jin, Y.; Fang, L.; Hu, B.; Dong, M. Activating MoS₂ with super-high nitrogen-doping concentration as efficient catalyst for hydrogen evolution reaction. *J. Phys. Chem. C* **2019**, *123*, 10917–10925. [[CrossRef](#)]
34. Bolar, S.; Shit, S.; Murmu, N.C.; Samanta, P.; Kuila, T. Activation strategy of MoS₂ as HER electrocatalyst through doping-induced lattice strain, band gap engineering, and active crystal plane design. *ACS Appl. Mater. Interfaces* **2021**, *13*, 765–780. [[CrossRef](#)]
35. Qin, S.; Lei, W.; Liu, D.; Chen, Y. Advanced N-doped mesoporous molybdenum disulfide nanosheets and the enhanced lithium-ion storage performance. *J. Mater. Chem. A* **2016**, *4*, 1440–1445. [[CrossRef](#)]
36. Shi, Y.; Zhou, Y.; Yang, D.-R.; Xu, W.-X.; Wang, C.; Wang, F.-B.; Xu, J.-J.; Xia, X.-H.; Chen, H.-Y. Energy level engineering of MoS₂ by transition-metal doping for accelerating hydrogen evolution reaction. *J. ACS* **2017**, *139*, 15479–15485. [[CrossRef](#)]
37. Guo, X.; Wan, X.; Liu, Q.; Li, Y.; Li, W.; Shui, J. Phosphated IrMo bimetallic cluster for efficient hydrogen evolution reaction. *Escience* **2022**, *2*, 304–310. [[CrossRef](#)]
38. Zhu, J.; Wang, Z.; Yu, H.; Li, N.; Zhang, J.; Meng, J.; Liao, M.; Zhao, J.; Lu, X.; Du, L. Argon plasma induced phase transition in monolayer MoS₂. *J. Am. Chem. Soc.* **2017**, *139*, 10216–10219. [[CrossRef](#)]
39. Wang, M.-Q.; Tang, C.; Ye, C.; Duan, J.; Li, C.; Chen, Y.; Bao, S.-J.; Xu, M. Engineering the nanostructure of molybdenum nitride nanodot embedded N-doped porous hollow carbon nanochains for rapid all pH hydrogen evolution. *J. Mater. Chem. A* **2018**, *6*, 14734–14741. [[CrossRef](#)]
40. Zhang, P.; Xu, B.; Chen, G.; Gao, C.; Gao, M. Large-scale synthesis of nitrogen doped MoS₂ quantum dots for efficient hydrogen evolution reaction. *Electrochim. Acta* **2018**, *270*, 256–263. [[CrossRef](#)]
41. Zhang, R.; Zhang, M.; Yang, H.; Li, G.; Xing, S.; Li, M.; Xu, Y.; Zhang, Q.; Hu, S.; Liao, H. Creating Fluorine-Doped MoS₂ Edge Electrodes with Enhanced Hydrogen Evolution Activity. *Small Methods* **2021**, *5*, 2100612. [[CrossRef](#)]
42. Xiao, Z.; Luo, S.; Duan, W.; Zhang, X.; Han, S.; Liu, Y.; Yang, L.; Lin, S. Doughty-electronegative heteroatom-induced defective MoS₂ for the hydrogen evolution reaction. *Front. Chem.* **2022**, *10*. [[CrossRef](#)]
43. Rivera, A.M.; Gaur, A.P.; Sahoo, S.; Katiyar, R.S. Studies on chemical charge doping related optical properties in monolayer WS₂. *J. Appl. Phys.* **2016**, *120*, 105102. [[CrossRef](#)]
44. Yang, X.; Yu, H.; Guo, X.; Ding, Q.; Pullerits, T.; Wang, R.; Zhang, G.; Liang, W.; Sun, M. Plasmon-exciton coupling of monolayer MoS₂-Ag nanoparticles hybrids for surface catalytic reaction. *Mater. Today Energy* **2017**, *5*, 72–78. [[CrossRef](#)]
45. Sunitha, A.; Hajara, P.; Shaji, M.; Jayaraj, M.; Saji, K. Luminescent MoS₂ quantum dots with reverse saturable absorption prepared by pulsed laser ablation. *J. Lumin.* **2018**, *203*, 313–321. [[CrossRef](#)]
46. Li, B.; Jiang, L.; Li, X.; Ran, P.; Zuo, P.; Wang, A.; Qu, L.; Zhao, Y.; Cheng, Z.; Lu, Y. Preparation of monolayer MoS₂ quantum dots using temporally shaped femtosecond laser ablation of bulk MoS₂ targets in water. *Sci. Rep.* **2017**, *7*, 1–12. [[CrossRef](#)]
47. Nguyen, V.; Dong, Q.; Yan, L.; Zhao, N.; Le, P.H. Facile synthesis of photoluminescent MoS₂ and WS₂ quantum dots with strong surface-state emission. *J. Lumin.* **2019**, *214*, 116554. [[CrossRef](#)]
48. Alexaki, K.; Kostopoulou, A.; Sygletou, M.; Kenanakis, G.; Stratakis, E. Unveiling the Structure of MoS_x Nanocrystals Produced upon Laser Fragmentation of MoS₂ Platelets. *ACS Omega* **2018**, *3*, 16728–16734. [[CrossRef](#)]

49. Madugundo, R.; Rao, N.V.R.; Schönhöbel, A.M.; Salazar, D.; El-Gendy, A.A. Recent developments in nanostructured permanent magnet materials and their processing methods. *Magn. Nanostruct. Mater.* **2018**, *1*, 157–198.
50. Chen, R.; Yang, C.; Cai, W.; Wang, H.-Y.; Miao, J.; Zhang, L.; Chen, S.; Liu, B. Use of platinum as the counter electrode to study the activity of nonprecious metal catalysts for the hydrogen evolution reaction. *ACS Energy Lett.* **2017**, *2*, 1070–1075. [[CrossRef](#)]
51. Cao, H.; Wang, H.; Huang, Y.; Sun, Y.; Shi, S.; Tang, M. Quantification of gold (III) in solution and with a test stripe via the quenching of the fluorescence of molybdenum disulfide quantum dots. *Microchim. Acta* **2017**, *184*, 91–100. [[CrossRef](#)]
52. Murugan, A.V.; Kale, B.; Kulkarni, A.V.; Kunde, L.B.; Saaminathan, V. Novel approach to control CdS morphology by simple microwave-solvothermal method. *J. Mater. Sci.* **2005**, *16*, 295–299. [[CrossRef](#)]
53. Tauc, J.; Grigorovici, R.; Vancu, A. Optical properties and electronic structure of amorphous germanium. *Phys. Status Solidi B* **1966**, *15*, 627–637. [[CrossRef](#)]
54. Dileep, K.; Sahu, R.; Sarkar, S.; Peter, S.C.; Datta, R. Layer specific optical band gap measurement at nanoscale in MoS₂ and ReS₂ van der Waals compounds by high resolution electron energy loss spectroscopy. *J. Appl. Phys.* **2016**, *119*, 114309. [[CrossRef](#)]
55. Mahdavi, M.; Kimiagar, S.; Abrinaei, F. Preparation of Few-Layered Wide Bandgap MoS₂ with Nanometer Lateral Dimensions by Applying Laser Irradiation. *Crystals* **2020**, *10*, 164. [[CrossRef](#)]
56. Ren, X.; Pang, L.; Zhang, Y.; Ren, X.; Fan, H.; Liu, S.F. One-step hydrothermal synthesis of monolayer MoS₂ quantum dots for highly efficient electrocatalytic hydrogen evolution. *J. Mater. Chem. A* **2015**, *3*, 10693–10697. [[CrossRef](#)]
57. Panchu, S.J.; Raju, K.; Swart, H.C.; Chokkalingam, B.; Maaza, M.; Henini, M.; Moodley, M.K. Luminescent MoS₂ quantum dots with tunable operating potential for energy-enhanced aqueous supercapacitors. *ACS Omega* **2021**, *6*, 4542–4550. [[CrossRef](#)]
58. Park, M.J.; Yi, S.-G.; Kim, J.H.; Yoo, K.-H. Metal–insulator crossover in multilayered MoS₂. *Nanoscale* **2015**, *7*, 15127–15133. [[CrossRef](#)]
59. Splendiani, A.; Sun, L.; Zhang, Y.; Li, T.; Kim, J.; Chim, C.-Y.; Galli, G.; Wang, F. Emerging photoluminescence in monolayer MoS₂. *Nano Lett.* **2010**, *10*, 1271–1275. [[CrossRef](#)]
60. Wang, D.; Li, X.-B.; Han, D.; Tian, W.Q.; Sun, H.-B. Engineering two-dimensional electronics by semiconductor defects. *Nano Today* **2017**, *16*, 30–45. [[CrossRef](#)]
61. Wu, Z.; Ni, Z. Spectroscopic investigation of defects in two-dimensional materials. *Nanophotonics* **2017**, *6*, 1219–1237. [[CrossRef](#)]
62. Kang, N.; Paudel, H.P.; Leuenberger, M.N.; Tetard, L.; Khondaker, S.I. Photoluminescence quenching in single-layer MoS₂ via oxygen plasma treatment. *J. Phys. Chem. C* **2014**, *118*, 21258–21263. [[CrossRef](#)]
63. Nan, H.; Wang, Z.; Wang, W.; Liang, Z.; Lu, Y.; Chen, Q.; He, D.; Tan, P.; Miao, F.; Wang, X. Strong photoluminescence enhancement of MoS₂ through defect engineering and oxygen bonding. *ACS Nano* **2014**, *8*, 5738–5745. [[CrossRef](#)]
64. Kwak, I.H.; Kwon, I.S.; Abbas, H.G.; Jung, G.; Lee, Y.; Debela, T.T.; Yoo, S.J.; Kim, J.-G.; Park, J.; Kang, H.S. Nitrogen-rich 1T'-MoS₂ layered nanostructures using alkyl amines for high catalytic performance toward hydrogen evolution. *Nanoscale* **2018**, *10*, 14726–14735. [[CrossRef](#)] [[PubMed](#)]
65. Sanjinés, R.; Wiemer, C.; Almeida, J.; Levy, F. Valence band photoemission study of the Ti Mo N system. *Thin Solid Films* **1996**, *290*, 334–338. [[CrossRef](#)]
66. Zhou, W.; Hou, D.; Sang, Y.; Yao, S.; Zhou, J.; Li, G.; Li, L.; Liu, H.; Chen, S. MoO₂ nanobelts@ nitrogen self-doped MoS₂ nanosheets as effective electrocatalysts for hydrogen evolution reaction. *J. Mater. Chem. A* **2014**, *2*, 11358–11364. [[CrossRef](#)]
67. Wu, F.-Y.; Cheng, Y.-S.; Wang, D.-M.; Li, M.-L.; Lu, W.-S.; Xu, X.-Y.; Zhou, X.-H.; Wei, X.-W. Nitrogen-doped MoS₂ quantum dots: Facile synthesis and application for the assay of hematin in human blood. *Mater. Sci. Eng. C* **2020**, *112*, 110898. [[CrossRef](#)]
68. Shuxian, Z.; Hall, W.K.; Ertl, G.; Knözinger, H. X-ray photoemission study of oxygen and nitric oxide adsorption on MoS₂. *Appl. Catal.* **1986**, *100*, 167–175. [[CrossRef](#)]
69. Baby, M.; Kumar, K.R. Synthesis and characterisation of MoS₂ quantum dots by liquid nitrogen quenching. *Mater. Sci. Technol.* **2019**, *35*, 1416–1427. [[CrossRef](#)]
70. Benoist, L.; Gonbeau, D.; Pfister-Guillouzo, G.; Schmidt, E.; Meunier, G.; Levasseur, A. XPS analysis of oxido-reduction mechanisms during lithium intercalation in amorphous molybdenum oxysulfide thin films. *Solid State Ion.* **1995**, *76*, 81–89. [[CrossRef](#)]
71. Anwar, M.; Hogarth, C.; Bulpett, R. Effect of substrate temperature and film thickness on the surface structure of some thin amorphous films of MoO₃ studied by X-ray photoelectron spectroscopy (ESCA). *J. Mater. Sci.* **1989**, *24*, 3087–3090. [[CrossRef](#)]
72. Kuo, D.-H.; Abdullah, H.; Gultom, N.S.; Hu, J.-Y. Ag-decorated MoS_x laminar-film electrocatalyst made with simple and scalable magnetron sputtering technique for hydrogen evolution: A defect model to explain the enhanced electron transport. *ACS Appl. Mater. Interfaces* **2020**, *12*, 35011–35021. [[CrossRef](#)] [[PubMed](#)]
73. Tang, P.; Jiao, J.; Fan, Q.; Wang, X.; Agrawal, V.; Xu, Q. Interlayer spacing engineering in N doped MoS₂ for efficient lithium ion storage. *Mater. Chem. Phys.* **2021**, *261*, 124166. [[CrossRef](#)]
74. Bayat, A.; Zirak, M.; Saievar-Iranizad, E. Vertically aligned MoS₂ quantum dots/nanoflakes heterostructure: Facile deposition with excellent performance toward hydrogen evolution reaction. *ACS Sustain. Chem. Eng.* **2018**, *6*, 8374–8382. [[CrossRef](#)]

75. Azcatl, A.; Qin, X.; Prakash, A.; Zhang, C.; Cheng, L.; Wang, Q.; Lu, N.; Kim, M.J.; Kim, J.; Cho, K. Covalent nitrogen doping and compressive strain in MoS₂ by remote N₂ plasma exposure. *Nano Lett.* **2016**, *16*, 5437–5443. [[CrossRef](#)] [[PubMed](#)]
76. Li, R.; Yang, L.; Xiong, T.; Wu, Y.; Cao, L.; Yuan, D.; Zhou, W. Nitrogen doped MoS₂ nanosheets synthesized via a low-temperature process as electrocatalysts with enhanced activity for hydrogen evolution reaction. *J. Power Sources* **2017**, *356*, 133–139. [[CrossRef](#)]

Disclaimer/Publisher's Note: The statements, opinions and data contained in all publications are solely those of the individual author(s) and contributor(s) and not of MDPI and/or the editor(s). MDPI and/or the editor(s) disclaim responsibility for any injury to people or property resulting from any ideas, methods, instructions or products referred to in the content.